5 Mechanical Stabilities and Properties of Graphene and Its Modification by BN Predicted from First-Principles Calculations

Qing Peng and Suvranu De

CONTENTS

ABSTRACT

We investigate the mechanical stabilities and properties of graphene under various strains using first-principles plane-wave calculations based on density functional theory. We report the mechanics dependence of the graphene-like boron nitride (*g*-BN) concentration, including the high-order elastic constants and mechanical failure. Acting anisotropically, a large nonlinear elastic deformation up to the ultimate strength of the material, followed by a strain softening is observed. The ultimate strains in heterogeneous configurations are smaller than those in pure graphene and *g*-BN, which is related to the heterogeneity of the *g*-BNC monolayer. The in-plane stiffness as well as third-order elastic constants of graphene can be linearly tuned with *g*-BN concentration. The fourth- and fifth-order elastic constants have a more complex response to BN modification. The longitudinal mode elastic constants are sensitive to the BN modification in contrast with the shear mode elastic constants. The third-, fourth-, and fifth-order elastic constants are required for accurate modeling of the mechanical properties of *g*-BNC under strains greater than 0.02, 0.06, and 0.12, respectively. This study may provide guidance in tuning the mechanical properties through chemical modification of graphene by BN to optimize the function of graphene-based nanodevices, as well as their safe ranges of strain for the demanded engineering.

5.1 INTRODUCTION

With sp^2 bonds in a monatomic layer, graphene presents marvelous electrical and mechanical properties as well as exciting applications [1–6]. However, graphene is not perfect: a zero bandgap limits its applications in field-effect transistors with high on-off ratios, as well as logic and high-speed switching devices, since the current can never be turned off completely [7–10]. A significant amount of research has been conducted in order to modify the graphene bandgap for electronics applications. Several methods have been proposed for this purpose; however, most of them can only improve the semiconducting properties of graphene up to a limited point [11,12]. The graphene analog of boron nitride (*g*-BN) has a large bandgap [13], indicating an efficient way to engineer the bandgap of graphene through chemical modification using *g*-BN [14–27]. Recently, a promising method has been reported in which atomistic monolayers have been generated consisting of *g*-BN phases in graphene (*g*-BNC, Figure 5.1) using a thermal catalytic chemical vapor deposition method [27–29]. An atomically thin integrated circuitry made of *g*-BNC was freshly reported [30]. These hybrid monolayers have been shown to have isotropic physical properties which can be tailored by controlling the kinetic factors affecting the *g*-BN domain size within the graphene layer. This is different from B-doped or N-doped graphene, where the integrity of

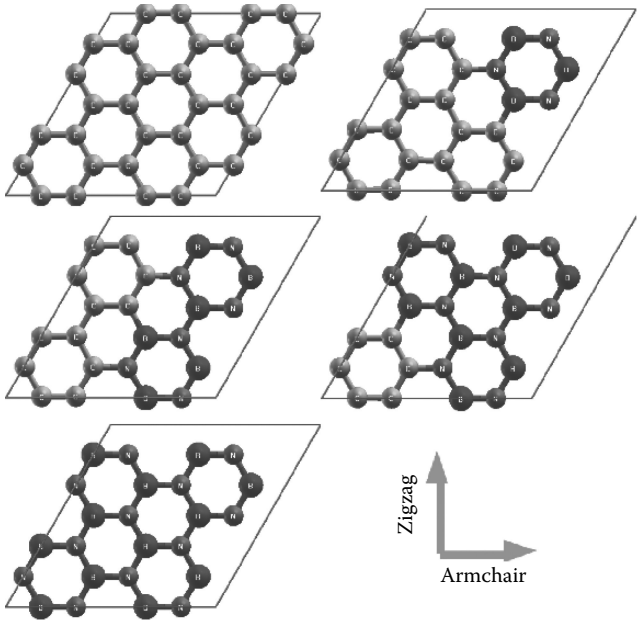

FIGURE 5.1 Atomic super cell (24 atoms) of five *g*-BNC configurations in undeformed reference configurations, corresponding to *g*-BN concentration of 0% (graphene), 25%, 50%, 75%, and 100% (*g*-BN).

the *g*-BN structure is missing. Opposed to *h*-BN, which is a bulk hexagonal structure, *g*-BNC and *g*-BN are only monoatomically thick. Compared with the electronic [13,31–33], optical [34], and optoelectronic properties [35], the mechanics dependence of the modification of graphene by *g*-BN is less studied.

Mechanical properties are critical in designing parts or structures with these advanced 2D nanomaterials regarding their practical applications, including high-frequency field-effect transistors [4], graphene-based spintronics [8], ferromagnetic [36], antiferromagnetics [37], mass sensors [38], and nanoelectronics [39]. Aside from electronic properties such as bandgaps [13], tunable mechanical properties can provide an optimal function in designing and manufacturing the graphene-based nano- or microelectronics. Furthermore, strain engineering is a common and important approach to tailor the functional and structural properties of nanomaterials [40]. In addition, these 2D materials are vulnerable to strain with or without intent because of the monatomic thickness [41,42]. For example, there are strains caused by the mismatch of lattices or surface corrugation due to the presence of a substrate [39,43]. Therefore, knowledge of the mechanical properties of modified graphene by *g*-BN (namely, *g*-BNC) is highly desired. Since graphene and *g*-BN are the lower and upper bounds of *g*-BNC (0% and 100% of *g*-BN concentration), we consider graphene and *g*-BN as a special case of *g*-BNC in this study.

Depending on the loading, the mechanical properties are divided into four strain domains: linear elastic, nonlinear elastic, plastic, and fracture. Materials in the first two strain domains are reversible, that is, they can return to equilibrium status after the release of the loads. On the other hand, the last two domains are nonreversible. Defects are nucleated and accumulate with the increase of the strain until rupture. The elastic properties of *g*-BNC within a small strain domain (±0.015) were reported recently [44]. However, particularly in graphene, the nonlinear mechanical properties are prominent since the nanoindentation tests strongly suggest that the graphene films were free from defects and remained elastic until the intrinsic strength was reached [45,46]. When the atomic displacement is no longer small with respect to the interatomic spacing, the anharmonicity of the crystal becomes noticeable and needs to be treated by the higher-order elasticity theory when the continuum approximation is adopted [47]. High-order elastic constants are important quantities [48–50] and can be determined by measuring the changes of sound velocities under the application of hydrostatic and uniaxial stresses [51,52]. The high-order elastic constants can be utilized to study the nonlinear elasticity [53], thermal expansion (through the Gruneisen parameter) [54], temperature dependence of elastic constants [54,55], harmonic generation [52], phonon–phonon interactions [56], photon–phonon interactions [57], lattice defects [58], phase transitions [59], echo phenomena [60], and so on. The study of the nonlinear elastic properties is necessary to understand the strength and reliability of structures and devices made of graphene and *g*-BNC.

The mechanical properties of graphene have been studied extensively [45,46,61], including theoretical predictions of the high-order elastic constants describing the nonlinear elastic properties [46,61]. These predictions are based on first-principles calculations in a unit cell containing two or four carbon atoms. However, it was reported that the finite wave vector soft modes, which are the key factors in limiting the strength of monolayer materials, can only be captured in unit cells with hexagonal rings [62]. Considering the overwhelming importance, the nonlinear elastic properties of graphene, *g*-BN, and *g*-BNC deserve a rigorous investigation.

The goal of this chapter is to study the dependence of mechanical behaviors on the *g*-BN concentration in *g*-BNC, in order to modulate the mechanics of graphene by BN. Our study also provides an accurate continuum description of the elastic properties of *g*-BNC, including nonlinear high-order elastic properties from density functional theory (DFT) calculations. The total energies of the system, forces on each atom, and stresses on the simulation boxes are directly obtained from DFT calculations. The response of *g*-BNC under the nonlinear deformation and fracture is studied, including ultimate strength and ultimate strain. The high-order elastic constants are obtained by fitting the stress–strain curves to analytical stress–strain relationships that belong to the continuum formulation [63]. The remainder of the chapter is organized as follows. Section 5.2 presents the computational details of DFT calculations. The results and analysis are in Section 5.3, followed by conclusions in Section 5.4.

5.2 DFT CALCULATIONS

In *g*-BNC materials, the *g*-BN phase is presented by the hexagonal structure of BN locally, which is a six-atom hexagonal

ring unit and can be denoted as (B_3N_3). The *g*-BN domain in *g*-BNC hybrid structures is modeled by adjusting the *g*-BN concentrations in *g*-BNC while maintaining the integrity of B_3N_3 within the system. The *g*-BN domain size in a system can be equivalently expressed by the *g*-BN concentration in the model as $(B_3N_3)_x(C_6)_{1-x}$ where (C_6) denotes the six-atom hexagonal ring unit of graphene. The six-atom hexagonal ring unit cell is chosen to capture the "soft mode," which is a particular normal mode exhibiting an anomalous reduction in its characteristic frequency and leading to mechanical instability. This soft mode is a key factor in limiting the strength of monolayer materials, and can only be captured in unit cells with hexagonal rings [62]. This *g*-BNC domain model was successfully used to study the electronic band structures and linear elastic properties of *g*-BNC heterostructures in our previous work [13,44].

The stress–strain relationship of *g*-BN under the desired deformation configurations is characterized via first-principles calculations based on DFT. DFT calculations were carried out within the Vienna Ab-initio Simulation Package [64,65] which is based on the Kohn–Sham DFT (KS-DFT) [66] with the generalized gradient approximations as parameterized by Perdew, Burke, and Ernzerhof for exchange–correlation functions [67]. The electrons explicitly included in the calculations are the ($2s^2p^1$) electrons of boron, the ($2s^22p^2$) electrons of carbon, and ($2s^22p^3$) electrons of nitrogen. The core electrons ($1s^2$) of boron, carbon, and nitrogen are replaced by the projector-augmented wave approach [68,69]. A plane-wave cutoff of 520 eV is used in all the calculations. The calculations are performed at zero temperature.

The criterion to stop the relaxation of the electronic degrees of freedom is set by requiring the total energy change to be smaller than 0.000001 eV. The optimized atomic geometry was achieved through minimizing Hellmann–Feynman forces acting on each atom until the maximum forces on the ions were smaller than 0.001 eV/Å.

The atomic structures of all the deformed and undeformed configurations are obtained by fully relaxing the 24-atom unit cells where all atoms are placed in one plane. Periodic boundary conditions are applied for the two in-plane directions.

The irreducible Brillouin zone was sampled with a gamma-centered $19 \times 19 \times 1$ *k*-mesh. Such a large *k*-mesh was used to reduce the numerical errors caused by the strain of the systems. The initial charge densities were taken as a superposition of atomic charge densities. There was a 14 Å thick vacuum region to reduce the interlayer interaction to model the single-layer system. To eliminate the artificial effect of the out-of-plane thickness of the simulation box on the stress, we used the second Piola–Kirchhoff (P–K) stress [63,70] to express the 2D forces per length with units of N/m.

For a general deformation state, the number of independent components of the second-, third-, fourth-, and fifth-order elastic tensors are 21, 56, 126, and 252, respectively. However, there are only 14 independent elastic constants that need to be explicitly considered due to the symmetries of the atomic lattice point group D_{6h}, which consists of a sixfold rotational axis and six mirror planes [46].

The 14 independent elastic constants of *g*-BNC are determined by a least-squares fit to the stress–strain results from DFT calculations in two steps, detailed in our previous work [63], which had been well used to explore the mechanical properties of 2D materials [26,71–82]. A brief introduction is that, in the first step, we use a least-squares fit of five stress–strain responses. Five relationships between stress and strain are necessary because there are five independent fifth-order elastic constants (FFOEC). We obtain the stress–strain relationships by simulating the following deformation states: uniaxial strain in the zigzag direction (zigzag); uniaxial strain in the armchair direction (armchair); and equibiaxial strain (biaxial). From the first step, the components of the second-order elastic constants (SOEC), the third-order elastic constants (TOEC), and the fourth-order elastic constants (FOEC) are overdetermined (i.e., the number of linearly independent variables is greater than the number of constraints), and the fifth-order elastic constants are well determined (the number of linearly independent variables are equal to the number of constraints). Under such circumstances, the second step is needed: the least-square solution to these over- and well-determined linear equations.

5.3 STRUCTURAL PROPERTIES

The optimized atomistic structures of the five configurations are shown in Figure 5.1, in ascending order of *g*-BN concentration as 0% (graphene), 25%, 50%, 75%, and 100% (*g*-BN). Owing to the intrinsic difference between pure *g*-BN and graphene, the lattice constants of the *g*-BNC mixtures are obtained by averaging the lattice vectors of the super cells for a direct comparison with pure *g*-BN and graphene. We found that the lattice constant increases with *g*-BN concentration x. Our results of the lattice constants are summarized in Table 5.1, which are in good agreement with experiments conducted on *g*-BN (2.51 Å) [83] and graphene (2.46 Å) [84].

When the strains are applied, all the atoms are allowed full freedom of motion. A quasi-Newton algorithm is used to relax all atoms into equilibrium positions within the deformed unit cell that yields the minimum total energy for the imposed strain state of the super cell.

Both compression and tension are considered here in order to sample a larger elastic deformation region. We study the behavior of the system under the Lagrangian strain ranged from −0.1 to 0.3 with an increment of 0.02 in each step in the three deformation modes for each configuration.

5.4 POTENTIAL SURFACES

Both compression and tension are considered with Lagrangian strains ranging from −0.1 to 0.3 with an increment of 0.02 in each step for all three deformation modes. The system's energy will increase when strains are applied. We define strain energy per atom $E_s = (E_{tot} - E_0)/n$, where E_{tot} is the total energy of the strained system, E_0 is the total energy of the strain-free system, and n is the number of atoms in the unit cell. This intensive quantity is used for the comparison

TABLE 5.1
Lattice Constants *a*, In-Plane Stiffness Y_s, Poisson Ratio ν, and High-Order Elastic Constants of *g*-BNC from DFT Calculations, Compared to Previous Calculations of Graphene

	0.0	0.25	0.5	0.75	1.00	Graphene[a]
a	2.468	2.484	2.496	2.506	2.512	2.446
Y_s	344.6	321.9	300.0	285.7	278.3	348
v	0.179	0.1839	0.1937	0.1998	0.2254	0.169
C_{11}	356	333.2	311.8	279.6	293.2	358.1
C_{12}	63.7	61.3	60.4	59.4	66.1	60.4
C_{111}	−3121	−2888	−2666	−2560	−2514	−2817
C_{112}	−472	−551	−407	−383	−425	−337
C_{222}	−2987	−2722	−2466	−2381	−2284	−2693
C_{1111}	19980	18220	20195	18030	16547	13416
C_{1112}	2706	3643	4267	2628	2609	759
C_{1122}	2843	4065	2012	6755	2215	2582.8
C_{2222}	16568	16085	19746	13234	12288	10358.9
C_{11111}	−80198	−77944	−130712	−98102	−65265	−31383.8
C_{11112}	−13378	−18430	−30317	−13725	−8454	−88.4
C_{11122}	−12852	29572	−52986	−62434	−28556	−12960.5
K_{12222}	−28504	−34777	−34287	−47317	−36955	−13046.6
K_{22222}	−79311	−146507	−328759	−121135	−100469	−33446.7

[a] Graphene in a 2-atom unit cell [45].

between different systems. Figure 5.2 shows the E_s as a function of strain in uniaxial armchair, uniaxial zigzag, and equibiaxial deformation.

E_s is seen to be anisotropic with strain direction, consistent with the nonisotropic structure of the monolayer *g*-BNC. E_s is nonsymmetrical for compression ($\eta < 0$) and tension ($\eta > 0$) for all three modes. This nonsymmetry indicates the anharmonicity of the *g*-BNC structures. The harmonic region, where the E_s is a quadratic function of applied strain, can be taken between $-0.02 < \eta < 0.02$. The stresses, derivatives of the strain energies, linearly increase with the increase of applied strains in the harmonic region. The anharmonic region is the range of strain where the linear stress–strain relationship is invalid, and higher-order terms are not negligible. With even larger loading of strains, the systems will undergo irreversible structural changes, and the systems are in a plastic region, where they might fail. The maximum strain before the failure is the critical strain. The ultimate strains are determined as the corresponding strain of the ultimate stress, which is the maxima of the stress–strain curve, as discussed in the following section.

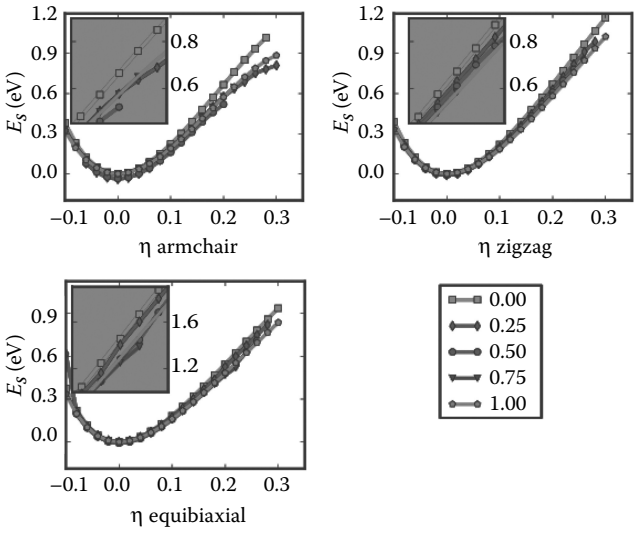

FIGURE 5.2 Energy–strain responses for uniaxial strain in armchair and zigzag directions, and equibiaxial strains as a function of *g*-BN concentrations.

5.5 STRESS–STRAIN RESPONSE

The stress–strain (second P–K stress) (Lagrangian strain) relationship for uniaxial strain in the armchair and zigzag, as well as biaxial, are shown in Figure 5.3. These stress–strain curves reflect the facts of the nonisotropic *g*-BNC atomic structures, in addition to the anharmonic responses in compression and tension. Overall, the stress increases with strain monotonically in all compression cases. The linear relationship between stress and strain is valid in strain from −0.02 to 0.02, which is the linear elastic region.

When the tensile strain is beyond 0.02, a nonlinear relationship of stress–strain occurs. There is a maximum stress when tensile strain becomes larger than 0.14 for all five configurations. We denote this maximum stress as ultimate strength and the corresponding strain as ultimate strain. The

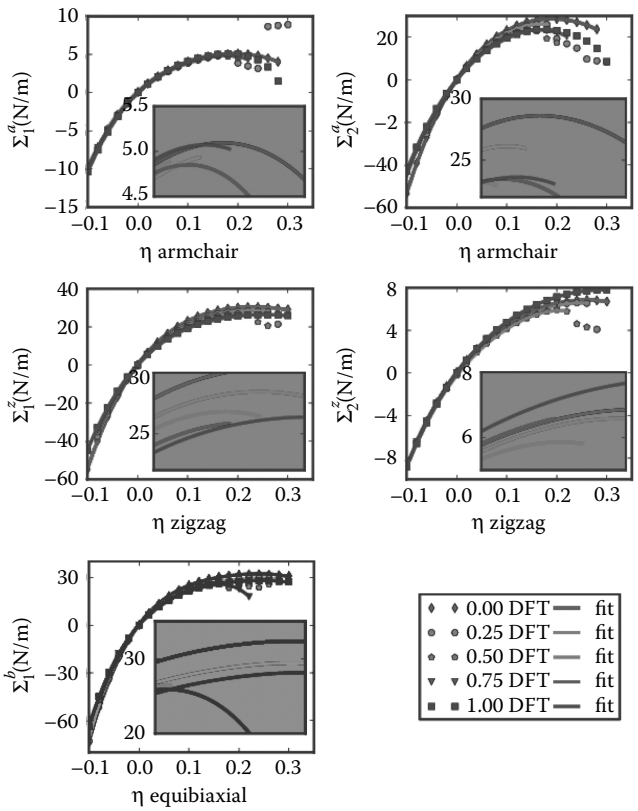

FIGURE 5.3 Stress–strain responses for uniaxial strain in armchair and zigzag directions, and equibiaxial strains as a function of *g*-BN concentrations C_{BN}. $\Sigma_1(\Sigma_2)$ denotes the x(y) component of stress. "fit" stands for the fitting of DFT calculations ("DFT") to continuum elastic theory.

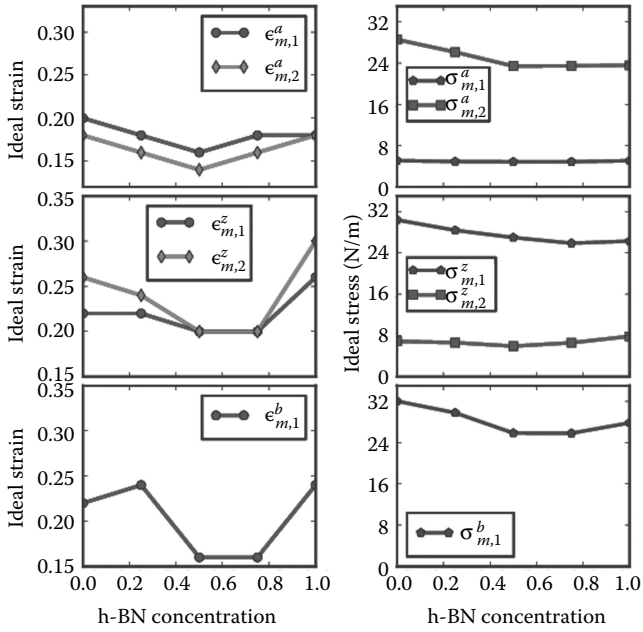

FIGURE 5.4 The ideal stress (ultimate stress) as well as the corresponding ideal (ultimate) strain at three deformation modes (armchair, zigzag, and equibiaxial) and two components (1,2) as a function of *g*-BN concentrations C_{BN}.

stress–strain curves of these five configurations are quite similar, due to their similar 2D hexagonal structures. As a consequence, the stress–strain curves are overlapped. The insets are zoomed-in plots showing different mechanical behaviors around the ultimate strains.

The stresses are the derivatives of the strain energies with respect to the strains. The ultimate strength (the maxima in the stress–strain curve) is the maximum stress that a material can withstand while being stretched, and the corresponding strain is the ultimate strain. Under ideal conditions, the critical strain is larger than the ultimate strain. The systems of *g*-BNC under strains beyond the ultimate strains are in a metastable state, which can be easily destroyed by long wavelength perturbations, vacancy defects, as well as high temperature effects [85]. The ultimate stress and strain are also called ideal stress and strain. The ultimate strain is determined by the intrinsic bonding strength that acts as a lower limit of the critical strain. Thus, it has practical meaning in consideration for its applications.

The ultimate stress and strain of all five configurations at three deformation modes are summarized and plotted in Figure 5.4 as a function of the *g*-BN concentrations C_{BN}. Please note that we use C_{BN} instead of x to represent the concentration of the *g*-BN phase in the rest of the chapter. We found that the ultimate strain of a certain configuration is a function of both deformation mode and the directions.

5.6 MECHANICAL FAILURES

When a heavy strain is applied, for example, 0.3 in this study, the system fails. Figure 5.5 shows the atomistic configurations of $C_{BN} = 0.25$ in the Lagrangian strain of 0.16 (shown in panels a, b, and c) and 0.30 (in panels d–f). The failure of the *g*-BNC of $C_{BN} = 0.25$ at uniaxial deformation along the armchair direction starts with the debonding of C–C bonds which are parallel to the direction of deformation. There are new bonds between N–N in this failure. This could be explained by the first-neighbor valence-bond model, introduced by Mazzoni et al. [86]. The first-neighbor bond energies between B, N, and C atoms from first-principle calculations are listed as follows (in units of eV) in descending order of the bond strength: $e_{NN} = -178.49$, $e_{CN} = -141.67$, $e_{BN} = -116.73$, $e_{CC} = -103.24$, $e_{CB} = -77.09$, $e_{BB} = -50.40$. There are four kinds of bonds in strain-free configurations of $C_{BN} = 0.25$: C–N, B–N, C–C, and C–B. We define a bond as broken when the bond length is 1.1 times of the original bond length. It is interesting that although the weakest bonds are C–B bonds, the C–C bonds along armchair, as marked in panel (a), break first. Owing to the intrinsic nonisotropic structure of *g*-BNC, applied strain on the system box will be distributed heterogeneously on these local bonds. It seems that the C–C bonds have higher strain concentrations and break prior to a C–B bond. At a strain of 0.3, as shown in panel (d), new B–B bonds and voids are generated after the failure.

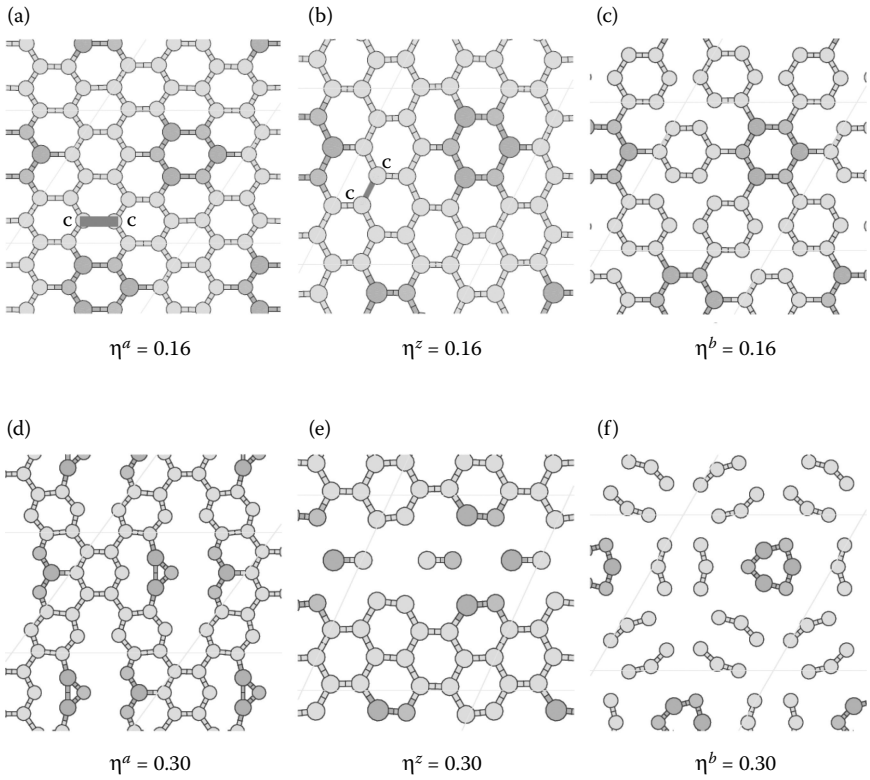

FIGURE 5.5 Atomic configurations of $C_{BN} = 0.25$ in the Lagrangian strain of 0.16 (a)–(c) and 0.30 (d)–(f).

For the uniaxial deformation along the armchair direction, the ultimate stress of $\Sigma_1^a = 5.08$ and $\Sigma_2^a = 23.56\,(\text{N/m})$ are at $\eta_a = 0.2$ and 0.18, respectively. For the uniaxial deformation along the zigzag, the maximum stresses are $\Sigma_1^z = 26.26\,(\text{N/m})$ at $\eta_z = 0.26$ and $\Sigma_2^z = 7.82\,(\text{N/m})$ at $\eta_z = 0.26$. In this case also, the C–C bonds, as marked in panel (b), break first, followed by the breaking of B–N bonds along zigzag. At a heavy strain of 0.3, as shown in panel (e), all bonds on *g*-BN along zigzag are broken. For the equibiaxial deformation, the maximum stresses are $\Sigma_1^b = \Sigma_2^b = 27.81(\text{N/m})$ at $\eta_b = 0.24$. C–C bonds that are parallel and next to B–N bonds break first, as shown in panel (c). At a heavy strain of 0.3, all C–B and C–N bonds are broken, as shown in panel (f).

For the *g*-BNC configuration at $C_{BN} = 0.5$, the B–N bonds along the armchair direction break first when the system deforms along the armchair direction, while the C–C bonds along zigzag break first during uniaxial zigzag and equibiaxial deformation, as shown in Figure 5.6. At a heavy strain of 0.3, the system breaks into pieces in all cases, as shown in Figure 5.6d through f.

For the *g*-BNC configuration at $C_{BN} = 0.75$, the C–N bonds along armchair break first when the system deforms along the armchair. The C–B bonds along zigzag break first during uniaxial, zigzag, and equibiaxial deformations, as shown in Figure 5.7. At a heavy strain of 0.3, the carbon atoms form "islands." There are voids in the *g*-BN domain during uniaxial armchair deformation, while the system breaks into pieces in the other two cases, as shown in Figure 5.7d through f.

For the pure graphene ($C_{BN} = 0.0$), there is only one kind of bond: C–C. The C–C bonds along the armchair break first during uniaxial armchair deformation. The C–C bonds along zigzag break first during uniaxial zigzag deformation. All bonds break simultaneously under equibiaxial deformation, as shown in Figure 5.8.

In the pure, *g*-BN ($C_{BN} = 1.0$), monolayer system, only the B–N bonds are present. Similar to pure graphene, the B–N bonds along the armchair break first during uniaxial armchair deformation; the B–N bonds along zigzag break first during uniaxial zigzag deformation; all bonds break simultaneously under equibiaxial deformation, as shown in Figure 5.9.

Figure 5.3 also shows that in all three deformation cases, both pure *g*-BN and graphene monolayers can withstand larger strains up to the point of failure, whilst the *g*-BNC structures break at lower strains. The failure behavior of *g*-BNC is highly anisotropic and is a function of the deformation direction and state, as well as *g*-BN concentration.

The strength of *g*-BNC heterostructures will decrease first, down to the minimum when $C_{BN} = 0.5$, and increase to that of pure *g*-BN, as shown in Figure 5.4. The nonisotropic nature of ultimate strain is more sensitive to the *g*-BN concentration in uniaxial strain along zigzag. The ultimate strength decreases with respect to the *g*-BN concentration.

There is a correlation between the debonding of structures shown in Figures 5.5 through 5.9 and ultimate strength (Figure 5.3). This indicates that the instabilities occur at debonding sites in the atomic structures. Therefore, the observed strain

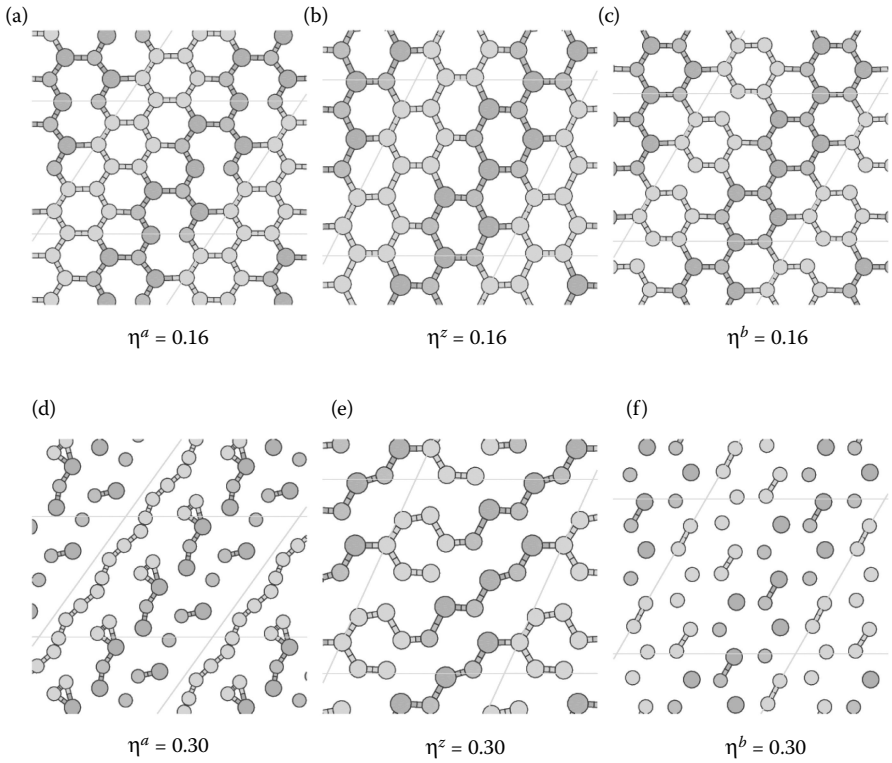

FIGURE 5.6 Atomic configurations of $C_{BN} = 0.5$ in the Lagrangian strain of 0.16 (a)–(c) and 0.30 (d)–(f).

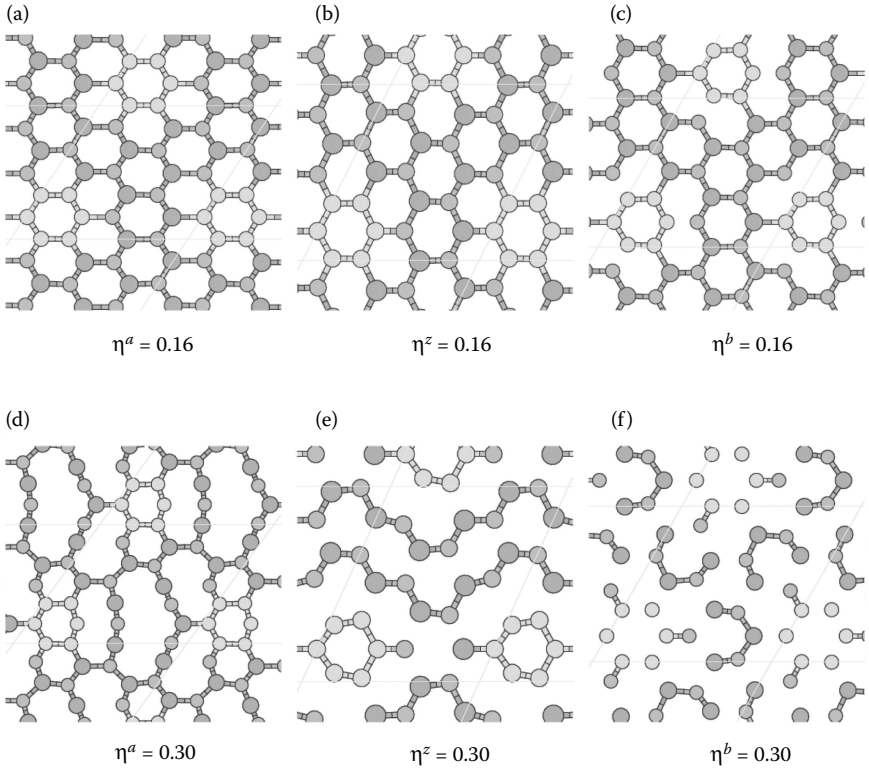

FIGURE 5.7 Atomic configurations of $C_{BN} = 0.75$ in the Lagrangian strain of 0.16 (a)–(c) and 0.30 (d)–(f).

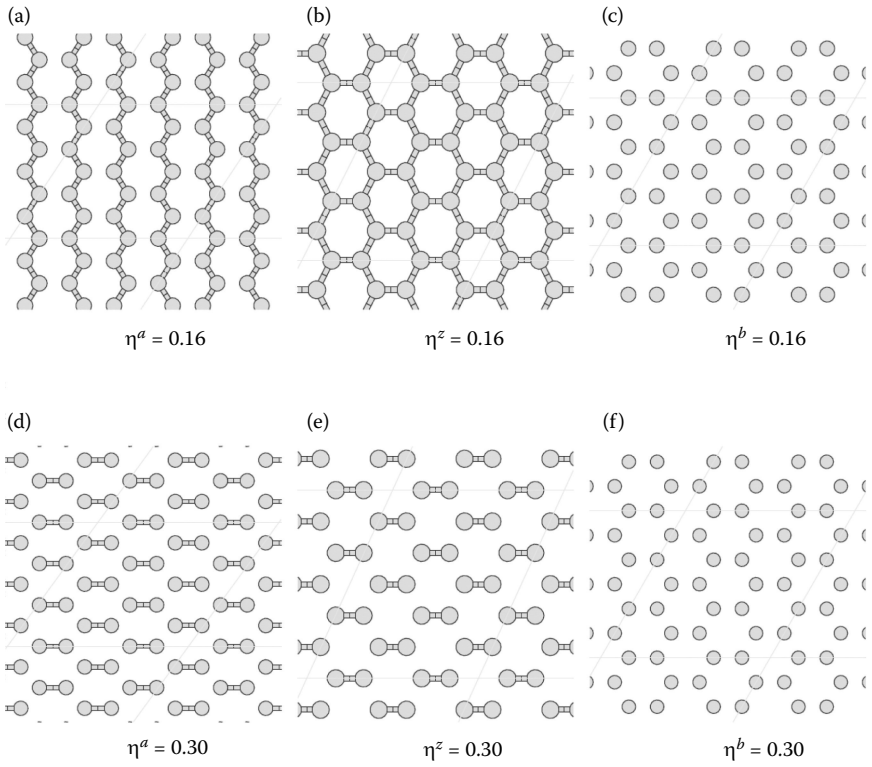

FIGURE 5.8 Atomic configurations of the pure graphene in the Lagrangian strain of 0.16 (a)–(c) and 0.30 (d)–(f).

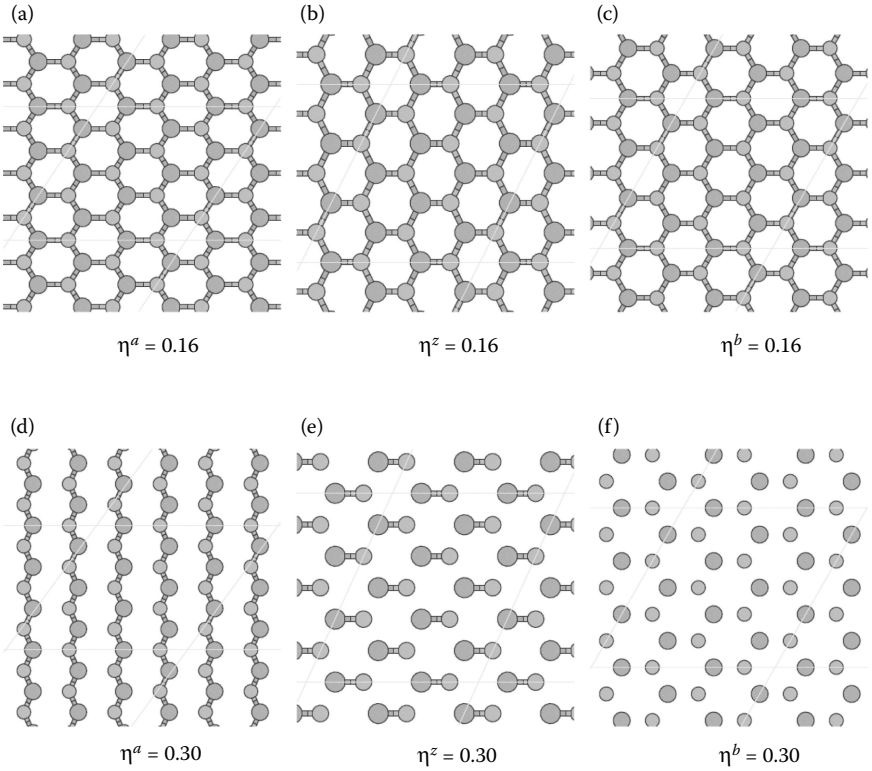

FIGURE 5.9 Atomic configurations of the pure *g*-BN in the Lagrangian strain of 0.16 (a)–(c) and 0.30 (d)–(f).

softening is due to the progressive debonding in the structure during stretching.

5.7 ELASTIC CONSTANTS

The elastic constants are essential to the continuum description of the elastic properties. The continuum responses are the least-square fit to the stress–strain results from the DFT calculations, as plotted in Figure 5.3. We then have 20 values for the 14 independent elastic constants of *g*-BNC from DFT calculations. The 14 independent elastic constants of *g*-BNC are determined by least-square fit to overdetermined equations [63]. The results of these 14 independent elastic constants are grouped in SOEC, TOEC, FOEC, and FFOEC as listed in Table 5.1.

Owing to the symmetry, only C_{11} and C_{12} are independent. C_{11} decreases linearly with respect to C_{BN}, as plotted in the top panel of Figure 5.10. The in-plane stiffness Ys Y_s can be obtained from the elastic moduli C_{11} and C_{12} as $Y_s = (C_{11}^2 - C_{12}^2)/C_{11}$. The Poisson ratio ν, which is the ratio of the transverse strain to the axial strain, can be obtained from elastic moduli as $\nu = C_{11}/C_{12}$. Our results of Y_s, ν and elastic constants of the five configurations are shown in the bottom panels of Figure 5.10. Our calculated value of in-plane stiffness of graphene (344.6 N/m) is in good agreement with the experimental value (340 ± 50 N/m) [45], and theoretical predictions (348 N/m [46] and 335 N/m [85]). Our calculated value of *g*-BN (278.3 N/m) agrees with an ab initio (GGA-PW91) prediction (267 N/m in Reference 85). Poisson ratios ν are 0.18 and 0.23 for graphene and *g*-BN, in agreement with 0.16 and 0.21, respectively [85]. Our results of Y_s, ν, C_{11}, and C_{12} are also comparable with ab initio predictions [87] and tight-binding calculations [88] of BN nanotubes.

We found that C_{11} and the in-plane stiffness decrease almost linearly as the *g*-BN concentration increases, while C_{12}, as well as the Poisson ratio ν, show a rather more complicated behavior (Figure 5.10). The similar trend of in-plane stiffness and C_{11} are based on the fact that C_{11} is dominant, about six times bigger than C_{12}. For the same reason, Poisson ratio ν has a similar trend as C_{12}. The increment of the Poisson ratio with respect to the *g*-BN concentration indicates a decrement of the network connectivity [89], consistent with the decrement of the density.

The effect of the *g*-BN concentration on the higher-order elastic constants is shown in Figure 5.11. In an overview, the third- and fifth-order elastic constants are all negative, in contrast with a positive FOEC. From the magnitude, the longitudinal modes (diagonal terms) of elastic constants are much larger than the shear modes (off-diagonal terms) of elastic constants. Comparing the elastic constants in different orders, one can notice that the TOEC of *g*-BNC vary mildly with the concentrations of *g*-BN. However, the fourth- and fifth-order elastic constants have a more complex response to the BN modification.

By considering the variation with respect to the BN concentration, we found that BN modification has a large effect on the longitudinal mode elastic constants, but is insensitive to the shear mode elastic constants. For the TOEC, the longitudinal modes C_{111} and C_{222} monotonically increase with respect to the *g*-BN concentration, as opposed to the small wiggles in the curve of shear mode C_{112}. The ratio of C_{111} to C_{112} is around six, same as the ratio of C_{11}/C_{12}. For the FOEC,

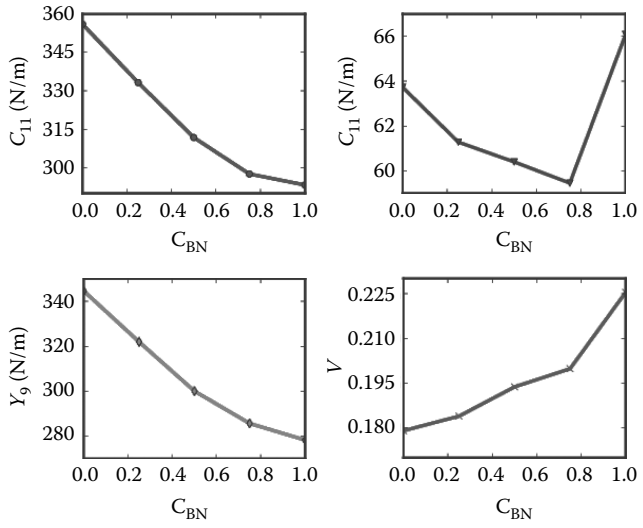

FIGURE 5.10 Linear elastic constants (SOEC) C11, C12, Y_s, and ν as a function of *g*-BN concentrations C_{BN}.

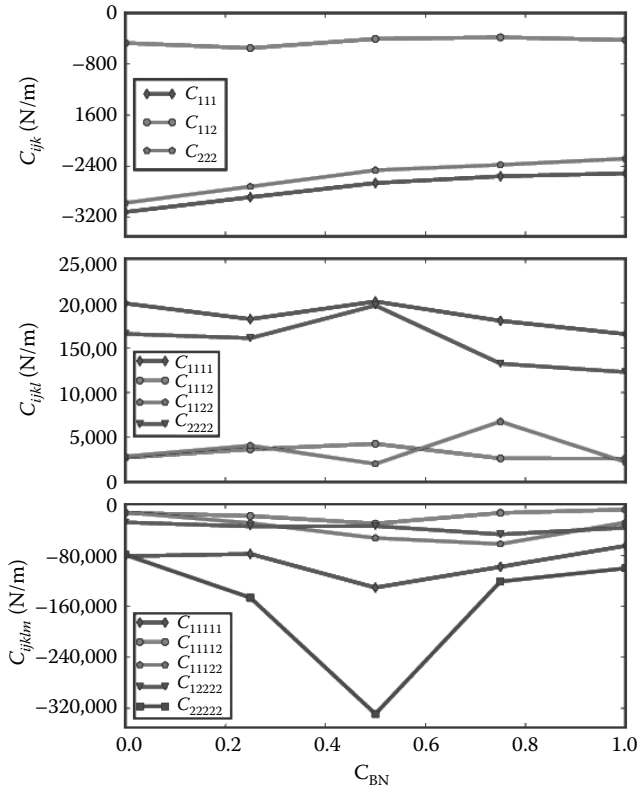

FIGURE 5.11 High-order elastic constants, TOEC, FOEC, and FFOEC as a function of *g*-BN concentrations C_{BN}.

the longitudinal modes C_{1111} and C_{2222} generally decease with respect to *g*-BN concentrations, with disturbances around $C_{BN} = 0.5$. The shear mode C_{1122} curve has larger fluctuations than the C_{1112}. For the fifth-order elastic constants, the longitudinal modes C_{1111} and C_{2222} are very sensitive to the *g*-BN concentration, with the minima at $C_{BN} = 0.5$. The shear modes C_{11112}, C_{11122}, and C_{12222} are relatively inert to the *g*-BN concentration. The valley points of C_{11111} and C_{22222} at $C_{BN} = 0.5$ indicate the instability of *g*-BNC around $C_{BN} = 0.5$. This is consistent with our previous observation of bond breaking.

As a comparison of the SOEC, our results of graphene agree with a previous study of using a 2-atom unit cell [46], as summarized in Table 5.1. However, there is considerable difference in the higher-order (>2) elastic constants. This is mainly because the primitive unit cell (2-atom unit cell) does not have the freedom to distort along the K1 mode (soft mode) as the primitive translational symmetry is enforced [62]. Such K1 soft mode is a precursor to a phase transition as in soft-mode theory, or directly leads to mechanical failure. This failure mechanism affects the nonlinear behavior of graphene around the ultimate strain, which is characterized by the high-order elastic constants.

The high-order elastic constants are strongly related to anharmonic properties, including thermal expansion, thermoelastic constants, and thermal conductivity. With higher-order elastic constants, we can easily study the pressure effect on the second-order elastic moduli, generalized Gruneisen parameters, and equations of states. For example, when pressure is applied, the pressure-dependent second-order elastic moduli can be obtained from C_{11}, C_{12}, C_{22}, C_{111}, C_{112}, C_{222}, Y_s, and ν [63,70,90,91]. In addition, using the higher-order elastic continuum description, one can obtain the mechanical behaviors under various loading conditions, for example, under applied stresses rather than strains as demonstrated in a previous study [46]. Furthermore, the high-order elastic constants are important in understanding the nonlinear elasticity of materials such as changes in acoustic velocities due to finite strain. As a consequence, nanodevices such as nanosurface acoustic wave sensors and nanowaveguides could be synthesized by introducing local strain [70].

A good way to check the importance of the high-order elastic constants is to consider the case when they are missing. With the elastic constants, the stress–strain response can be predicted from the elastic theory [63]. We take the configuration of the *g*-BNC with $C_{BN} = 0.25$ as an example to demonstrate here. When we only consider the second-order elasticity, the stress varies with strain linearly. As illustrated in Figure 5.12, the linear behaviors are only valid within a small strain range, about $-0.02 \le \eta \le 0.02$, in the three deformation directions. With the knowledge of the elastic constants up to the third order, the stress–strain curve can be accurately predicted within the range of $-0.06 \le \eta \le 0.06$. Using the elastic constants up to the fourth order, the mechanical behaviors can be well treated up to a strain as great as 0.12. For the strains beyond 0.12, the fifth-order elastic constants are required for an accurate modeling. The analysis of the other configurations comes to the same results.

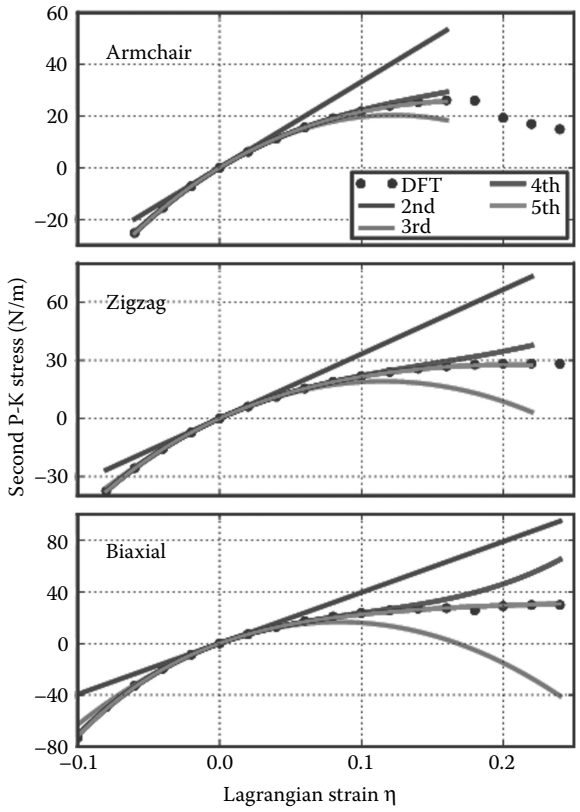

FIGURE 5.12 The predicted stress–strain responses from different orders: second, third, fourth, and fifth order, and compared with the DFT calculations in the three deformation directions of $C_{BN} = 0.25$.

Our results illustrate that the monatomic layer structures possess different mechanical behaviors in contrast with the bulk or multilayered structures, where the SOECs are sufficient in most cases. The SOECs are relatively easier to be calculated from the strain energy curves [18,85], however, they are not sufficient. The high-order elastic constants are required for an accurate description of the mechanical behaviors of monatomic layer structures since they are vulnerable to strain due to the geometrical confinements.

The *g*-BNC heterostructures are unstable under large tension. All stress–strain curves in the previous section show that such types of material will soften when the strain is greater than the ultimate strain. From the viewpoint of chemical bonding, this is due to the bond breaking. This softening behavior is determined by the high-order elastic constants. The high-order elastic constants reflect the high-order nonlinear bond strength under heavy strains. The negative values of FFOECs ensure the softening of materials under heavy strain beyond ultimate strains. The salient large values of FFOECs of $C_{BN} = 0.5$ *g*-BNC structure in Figure 5.11 make it easier to soften at heavy strains, indicating less stability.

Our results of mechanical properties of *g*-BNC are limited to zero temperature due to current DFT calculations. Once the finite temperature is considered, the thermal expansions and dynamics will, in general, reduce the interactions between atoms. As a result, the longitudinal mode elastic constants

will decrease with respect to the temperature of the system. The variation of shear mode elastic constants should be more complex in responding to the temperature. A thorough study will be interesting, which is, however, beyond the scope of this study.

5.8 CONCLUSIONS

In summary, we proposed an accurate approach to chemically tuning the mechanics of graphene with that of BN. Using a *g*-BNC domain model of $(B_3N_3)_x(C_6)_{1-x}$, we studied the concentration dependence of the mechanical properties of the hybrid graphene/boron nitride monolayer through first-principles calculations based on DFT. The nonlinear elasticity of *g*-BNC was investigated by applying large deformations. The continuum description of the elastic response is formulated by expanding the elastic strain energy density in a Taylor series of strain truncated after the fifth-order term. We obtained a total of 14 nonzero independent elastic constants for up to the tenth-order tensor for each examined *g*-BNC structure. The elastic constants (including those in high orders) are useful to develop an accurate continuum description of mechanical behaviors.

The results of the DFT calculations for the three deformation modes of zigzag, armchair, and biaxial revealed that graphene, *g*-BN, and *g*-BNC monolayers have anisotropic deformations and failure behaviors. The ultimate strength is also highly anisotropic in these monolayers, and changed with the *g*-BN concentrations. The ultimate strains are smaller in *g*-BNC heterogeneous monolayers than those in homogeneous monolayers, graphene and *g*-BN, which may be related to the heterogeneity of the *g*-BNC monolayer. The failure mechanism, from the viewpoint of the bond strength was studied. In pure graphene and the 25% *g*-BN system, C–C bonds along the loading direction break first. For the 50% *g*-BN system, B–N bonds along the armchair break first in armchair deformation, while C–N bonds along the zigzag break first in zigzag and equibiaxial deformation. For the 75% *g*-BN system, C–N bonds along the armchair break first in armchair deformation, while C–B bonds along the zigzag break first in zigzag and equibiaxial deformation. In pure *g*-BN system, B–N bonds along the loading direction break first.

The results show that the in-plane stiffness as well as TOECs of graphene can be linearly tuned with *g*-BN concentration. The longitudinal modes of elastic constants of *g*-BNC are much larger than the shear modes of elastic constants. The TOECs of *g*-BNC vary mildly with the concentrations of *g*-BN. However, the fourth- and fifth-order elastic constants have a more complex response to BN modification. BN modification has a large effect on the longitudinal mode elastic constants, but is insensitive to the shear mode elastic constants. We also find that the harmonic elastic constants are only valid with a small range of $-0.02 \le \eta \le 0.02$. With the knowledge of the elastic constants up to the third order, the stress–strain curve can be accurately predicted within the range of $-0.06 \le \eta \le 0.06$. Using the elastic constants up to the fourth order, the mechanical behaviors can be accurately predicted up to a strain as heavy as 0.12. For the strains beyond 0.12, the fifth-order elastic constants are required for an accurate modeling. The high-order elastic constants reflect the high-order nonlinear bond strength under large strains. The salient large values of FFOECs of the $C_{BN} = 0.5$ *g*-BNC structure make it easier to soften at heavy strains, indicating less stability. Our results may provide guidance in chemically tuning the mechanical properties of these heterostructures in practical applications, as well as the safe ranges of strain for the demanded engineering of the *g*-BNC.

ACKNOWLEDGMENTS

The authors would like to acknowledge the generous financial support from the Defense Threat Reduction Agency (DTRA) Grant # BRBAA08-C-2-0130 and # HDTRA1-13-1-0025.

REFERENCES

1. K. S. Novoselov, A. K. Geim, S. V. Morozov, D. Jiang, Y. Zhang, S. V. Dubonos, I. V. Grigorieva, and A. A. Firsov. Electric field effect in atomically thin carbon films. *Science*, 306(5696):666, Oct 22, 2004.
2. K. S. Novoselov, A. K. Geim, S. V. Morozov, D. Jiang, M. I. Katsnelson, I. V. Grigorieva, S. V. Dubonos, and A. A. Firsov. Two-dimensional gas of massless Dirac fermions in graphene. *Nature*, 438(7065):197–200, Nov 10, 2005.
3. Y.-M. Lin, K. A. Jenkins, A. Valdes-Garcia, J. P. Small, D. B. Farmer, and P. Avouris. Operation of graphene transistors at gigahertz frequencies. *Nano Lett.*, 9(1):422–426, Jan 2009.
4. Y. M. Lin, C. Dimitrakopoulos, K. A. Jenkins, D. B. Farmer, H. Y. Chiu, A. Grill, and P. Avouris. 100-GHz transistors from wafer-scale epitaxial graphene. *Science*, 327(5966):662, Feb 5, 2010.
5. L. Liao, Y.-C. Lin, M. Bao, R. Cheng, J. Bai, Y. Liu, Y. Qu, K. L. Wang, Y. Huang, and X. Duan. High-speed graphene transistors with a self-aligned nanowire gate. *Nature*, 467(7313):305–308, Sep 16, 2010.
6. M.-B. Ruben, G.-N. Cristina, G.-H. Julio, and Z. Felix. 2d materials: To graphene and beyond. *Nanoscale*, 3:20–30, 2011.
7. K. S. Novoselov, D. Jiang, F. Schedin, T. J. Booth, V. V. Khotkevich, S. V. Morozov, and A. K. Geim. Two-dimensional atomic crystals. *Proc. Nat. Acad. Sci. USA*, 102(30):10451–10453, Jul 26, 2005.
8. Y. Ma, Y. Dai, M. Guo, and B. Huang. Graphene-diamond interface: Gap opening and electronic spin injection. *Phys. Rev. B*, 85:235448, Jun 2012.
9. G. Brumfiel. Graphene gets ready for the big time. *Nature*, 458(7237):390–391, Mar 26, 2009.
10. T. P. Kaloni, Y. C. Cheng, and U. Schwingenschloegl. Electronic structure of superlattices of graphene and hexagonal boron nitride. *J. Mater. Chem.*, 22(3):919–922, 2012.
11. T. B. Martins, R. H. Miwa, A. J. R. da Silva, and A. Fazzio. Electronic and transport properties of boron-doped graphene nanoribbons. *Phys. Rev. Lett.*, 98(19):196803, May 2007.
12. A. Lherbier, X. Blase, Y.-M. Niquet, F. Triozon, and S. Roche. Charge transport in chemically doped 2d graphene. *Phys. Rev. Lett.*, 101(3):036808, Jul 2008.
13. Q. Peng and S. De. Tunable band gaps of mono-layer hexagonal BNC heterostructures. *Physica E*, 44:1662–1666, Apr 2012.

14. J. N. Coleman, M. Lotya, A. O'Neill, S. D. Bergin, P. J. King, U. Khan et al. Two-dimensional nanosheets produced by liquid exfoliation of layered materials. *Science*, 331(6017):568–571, 2011.
15. A. Nag, K. Raidongia, K. P. S. S. Hembram, R. Datta, U. V. Waghmare, and C. N. R. Rao. Graphene analogues of bn: Novel synthesis and properties. *ACS Nano*, 4(3):1539, Mar 2010.
16. C. Li, Y. Bando, C. Zhi, Y. Huang, and D. Golberg. Thickness-dependent bending modulus of hexagonal boron nitride nanosheets. *Nanotechnology*, 20(38):385707, Sep 23, 2009.
17. L. Song, L. Ci, H. Lu, P. B. Sorokin, C. Jin, J. Ni, A. G. Kvashnin et al. Large scale growth and characterization of atomic hexagonal boron nitride layers. *Nano Lett.*, 10(8):3209–3215, 2010.
18. M. Topsakal, E. Aktürk, and S. Ciraci. First-principles study of two- and one-dimensional honeycomb structures of boron nitride. *Phys. Rev. B*, 79(11):115442, Mar 2009.
19. K. Watanabe, T. Taniguchi, and H. Kanda. Direct-bandgap properties and evidence for ultraviolet lasing of hexagonal boron nitride single crystal. *Nat. Mater.*, 3(6):404, Jun 2004.
20. C. Zhi, Y. Bando, C. Tang, H. Kuwahara, and D. Golberg. Large-scale fabrication of boron nitride nanosheets and their utilization in polymeric composites with improved thermal and mechanical properties. *Adv. Mater.*, 21(28):2889, Jul 7, 2009.
21. M. Kawaguchi, T. Kawashima, and T. Nakajima. Syntheses and structures of new graphite-like materials of composition bcn(h) and bc3n(h). *Chem. Mater.*, 8(6):1197–1201, 1996.
22. K. Suenaga, C. Colliex, N. Demoncy, A. Loiseau, H. Pascard, and F. Willaime. Synthesis of nanoparticles and nanotubes with well-separated layers of boron nitride and carbon. *Science*, 278(5338):653–655, 1997.
23. W. Q. Han, W. Mickelson, J. Cumings, and A. Zettl. Transformation of bxcynz nanotubes to pure BN nanotubes. *Appl. Phys. Lett.*, 81(6):1110–1112, 2002.
24. T. Kawasaki, T. Ichimura, H. Kishimoto, A. A. Akbar, T. Ogawa, and C. Oshima. Double atomic layers of graphene/monolayer h-BN on Ni(111) studied by scanning tunneling microscopy and scanning tunneling spectroscopy. *Surf. Rev. Lett.*, 9(3–4):1459–1464, Jun–Aug 2002.
25. Q. Tang, Z. Zhou, and Z. Chen. Molecular charge transfer: A simple and effective route to engineer the band structures of BN nanosheets and nanoribbons. *J. Phys. Chem. C*, 115(38):18531–18537, Sep 29, 2011.
26. Q. Peng, W. Ji, and S. De. First-principles study of the effects of mechanical strains on the radiation hardness of hexagonal boron nitride monolayers. *Nanoscale*, 5:695–703, 2013.
27. L. Ci, L. Song, C. Jin, D. Jariwala, D. Wu, Y. Li, A. Srivastava et al. Atomic layers of hybridized boron nitride and graphene domains. *Nat. Mater.*, 9(5):430–435, May 2010.
28. J. da Rocha Martins and H. Chacham. Disorder and segregation in b-c-n graphene-type layers and nanotubes: Tuning the band gap. *ACS Nano*, 5(1):385, 2011.
29. S. Bhowrnick, A. K. Singh, and B. I. Yakobson. Quantum dots and nanoroads of graphene embedded in hexagonal boron nitride. *J. Phys. Chem. C*, 115(20):9889, 2011.
30. M. P. Levendorf, C.-J. Kim, L. Brown, P. Y. Huang, R. W. Havener, D. A. Muller, and J. Park. Graphene and boron nitride lateral heterostructures for atomically thin circuitry. *Nature*, 488(7413):627–632, Aug 30, 2012.
31. Y. Ding, Y. Wang, and J. Ni. Electronic properties of graphene nanoribbons embedded in boron nitride sheets. *Appl. Phys. Lett.*, 95(12):123105, 2009.
32. J. Li and V. B. Shenoy. Graphene quantum dots embedded in hexagonal boron nitride sheets. *Appl. Phys. Lett.*, 98(1):013105, 2011.
33. Y. Liu, X. Wu, Y. Zhao, Xiao Cheng Zeng, and J. Yang. Half-metallicity in hybrid graphene/boron nitride nanoribbons with dihydrogenated edges. *J. Phys. Chem. C*, 115(19):9442–9450, May 19, 2011.
34. H. Park, A. Wadehra, J. W. Wilkins, and A. H. Castro Neto. Magnetic states and optical properties of single-layer carbon-doped hexagonal boron nitride. *Appl. Phys. Lett.*, 100(25):253115, 2012.
35. M. Bernardi, M. Palummo, and J. C. Grossman. Optoelectronic properties in monolayers of hybridized graphene and hexagonal boron nitride. *Phys. Rev. Lett.*, 108:226805, Jun 2012.
36. Y. Ma, Y. Dai, M. Guo, C. Niu, Y. Zhu, and B. Huang. Evidence of the existence of magnetism in pristine vx2 monolayers (x = s, se) and their strain-induced tunable magnetic properties. *ACS Nano*, 6(2):1695–1701, 2012.
37. Y. Ma, Y. Dai, M. Guo, C. Niu, J. Lu, and B. Huang. Electronic and magnetic properties of perfect, vacancy-doped, and nonmetal adsorbed mose2, mote2 and ws2 monolayers. *Phys. Chem. Chem. Phys.*, 13:15546–15553, 2011.
38. S. Y. Kim and H. S. Park. On the utility of vacancies and tensile strain-induced quality factor enhancement for mass sensing using graphene monolayers. *Nanotechnology*, 21(10):105710, Mar 12, 2010.
39. Y. Ma, Y. Dai, W. Wei, C. Niu, L. Yu, and B. Huang. First-principles study of the graphene@MoSe2 heterobilayers. *J. Phys. Chem. C*, 115(41):20237–20241, Oct 20, 2011.
40. F. Guinea, M. I. Katsnelson, and A. K. Geim. Energy gaps and a zero-field quantum Hall effect in graphene by strain engineering. *Nat. Phys.*, 6(1):30–33, Jan 2010.
41. Q. Peng, J. Crean, A. Dearden, C. Huang, X. Wen, S. P. A. Bordas, and S. De, Defect engineering of 2D monatonic-layer materials. *Modern Phys. Lett. B*, 27:1330017, 2013.
42. Q. Peng, A. Dearden, J. Crean, L. Han, S. Liu, X. Wen, and S. De, New materials graphyne, graphdiyne, graphone, and graphane: Review of properties, synthesis, and application in nanotechnology. *Nanotechnol. Sci. Appl.*, 7:1–29, 2014.
43. Z. H. Aitken and R. Huang. Effects of mismatch strain and substrate surface corrugation on morphology of supported monolayer graphene. *J. Appl. Phys.*, 107(12):123531, Jun 15, 2010.
44. Q. Peng, A. R. Zamiri, W. Ji, and S. De. Elastic properties of hybrid graphene/boron nitride monolayer. *Acta Mechanica*, 223:2591–2596, 2012.
45. C. Lee, X. Wei, J. W. Kysar, and J. Hone. Measurement of the elastic properties and intrinsic strength of monolayer graphene. *Science*, 321(5887):385, 2008.
46. X. Wei, B. Fragneaud, C. A. Marianetti, and J. W. Kysar. Nonlinear elastic behavior of graphene: Ab initio calculations to continuum description. *Phys. Rev. B*, 80(20):205407, Nov 2009.
47. G. Leibfried and W. Ludwig. Theory of anharmonic effects in crystals. *Solid State Phys.*, 12:275–444, 1961.
48. R. N. Thurston and K. Brugger. Third-order elastic constants + velocity of small amplitude elastic waves in homogeneously stressed media. *Phys. Rev. A*, 133(6A):1604, 1964.
49. K. Brugger. Thermodynamic definition of higher order elastic coefficients. *Phys. Rev. A*, 133(6A):1611, 1964.
50. Y. Hiki. Higher-order elastic-constants of solids. *Annu. Rev. Mater. Sci.*, 11:51, 1981.
51. K. Brugger. Determination of 3rd-order elastic coefficients in crystals. *J. Appl. Phys.*, 36(3P1):768, 1965.

52. W. B. Gauster and M. A. Breazeale. Ultrasonic measurement of the nonlinearity parameters of copper single crystals. *Phys. Rev.*, 168:655–661, Apr 1968.
53. H. Kobayashi and Y. Hiki. Anharmonicity in noble metals; nonlinear elasticity in whiskers. *Phys. Rev. B*, 7:594–601, Jan 1973.
54. Y. Hiki, J. F. Thomas, and A. V. Granato. Anharmonicity in noble metals: Some thermal properties. *Phys. Rev.*, 153:764–771, Jan 1967.
55. J. A. Garber and A. V. Granato. Theory of the temperature dependence of second-order elastic constants in cubic materials. *Phys. Rev. B*, 11:3990–3997, May 1975.
56. W. P. Mason and T. B. Bateman. Relation between 3rd-order elastic moduli and thermal attenuation of ultrasonic waves in nonconducting and metallic crystals. *J. Acoust. Soc. Am.*, 40(4):852, 1966.
57. J. Melngailis, A. A. Maradudin, and A. Seeger. Diffraction of light by ultrasound in anharmonic crystals. *Phys. Rev.*, 131:1972–1975, Sep 1963.
58. A. D. Brailsfo. Anharmonicity contributions to dislocation drag. *J. Appl. Phys.*, 43(4):1380, 1972.
59. M. Wuttig and T. Suzuki. Non-linear anelasticity and the martensitic-transformation. *Acta Metall.*, 27(5):755–761, 1979.
60. K. Fossheim, K. Kajimura, T. G. Kazyaka, R. L. Melcher, and N. S. Shiren. Dynamic polarization echoes in piezoelectric powders. *Phys. Rev. B*, 17:964–998, Feb 1978.
61. F. Liu, P. Ming, and J. Li. Ab initio calculation of ideal strength and phonon instability of graphene under tension. *Phys. Rev. B*, 76(6):064120, Aug 2007.
62. C. A. Marianetti and H. G. Yevick. Failure mechanisms of graphene under tension. *Phys. Rev. Lett.*, 105:245502, 2010.
63. Q. Peng, W. Ji, and S. De. Mechanical properties of the hexagonal boron nitride monolayer: Ab initio study. *Comput. Mater. Sci.*, 56:11, 2012.
64. G. Kresse and J. Hafner. Ab initio molecular dynamics for liquid metals. *Phys. Rev. B*, 47:558, 1993.
65. G. Kresse and J. Furthuller. Efficiency of ab-initio total energy calculations for metals and semiconductors using a plane-wave basis set. *Comput. Mater. Sci.*, 6:15, 1996.
66. W. Kohn and L. J. Sham. Self-consistent equations including exchange and correlation effects. *Phys. Rev.*, 140(4A):A1133, Nov 1965.
67. J. Perdew, K. Burke, and M. Ernzerhof. Generalized gradient approximation made simple. *Phys. Rev. Lett.*, 77:3865, 1996.
68. P. E. Blöchl. Projector augmented-wave method. *Phys. Rev. B*, 50(24):17953–17979, Dec 1994.
69. R. O. Jones and O. Gunnarsson. The density functional formalism, its applications and prospects. *Rev. Mod. Phys.*, 61(3):689–746, Jul 1989.
70. Q. Peng, W. Ji, and S. De. Mechanical properties of graphyne monolayer: A first-principles study. *Phys. Chem. Chem. Phys.*, 14:13385–13391, 2012.
71. Q. Peng, C. Liang, W. Ji, and S. De. A first principles investigation of the mechanical properties of *g*-TlN. *Model. Numer. Simul. Mater. Sci.*, 2:76–84, 2012.
72. Q. Peng, C. Liang, W. Ji, and S. De. A first principles investigation of the mechanical properties of *g*-ZnO: The graphene-like hexagonal zinc oxide monolayer. *Comput. Mater. Sci.*, 68:320–324, 2013.
73. Q. Peng, C. Liang, W. Ji, and S. De. A theoretical analysis of the effect of the hydrogenation of graphene to graphane on its mechanical properties. *Phys. Chem. Chem. Phys.*, 15:2003–2011, 2013.
74. Q. Peng, X.-J. Chen, S. Liu, and S. De. Mechanical stabilities and properties of graphene-like aluminum nitride predicted from first-principles calculations. *RSC Adv.*, 3:7083–7092, 2013.
75. Q. Peng, C. Liang, W. Ji, and S. De. A first-principles study of the mechanical properties of *g*-GeC. *Mech. Mater.*, 64:135–141, 2013.
76. Q. Peng, C. Liang, W. Ji, and S. De. Mechanical properties of *g*-GaN: A first principles study. *Appl. Phys. A*, 13:483–490, 2013.
77. Q. Peng, X.-J. Chen, W. Ji, and S. De. Chemically tuning mechanics of graphene by BN. *Adv. Eng. Mater.*, 15:718–727, 2013.
78. Q. Peng, X. Wen, and S. De. Mechanical stabilities of silicene. *RSC Adv.*, 3:13772–13781, 2013.
79. Q. Peng, Z. Chen, and S. De. A density functional theory study of the mechanical properties of graphane with van der Waals corrections. *Mech. Adv. Mater. Struc.*, 22:717–721, 2015.
80. Q. Peng and S. De. Outstanding mechanical properties of monolayer MoS2 and its application in elastic energy storage. *Phys. Chem. Chem. Phys.*, 15:19427–19437, 2013.
81. Q. Peng and S. De, Elastic limits of silicane. *Nanoscale*, B:12071–12079, 2014.
82. Q. Peng and S. De, Mechanical properties and instabilities of ordered graphene oxide C6O monolayers, *RSC Adv.*, 3:24337–24344, 2013
83. L. Liu, Y. P. Feng, and Z. X. Shen. Structural and electronic properties of h-bn. *Phys. Rev. B*, 68(10):104102, Sep 2003.
84. Y. Baskin and L. Meyer. Lattice constants of graphite at low temperatures. *Phys. Rev.*, 100(2):544, 1955.
85. M. Topsakal, S. Cahangirov, and S. Ciraci. The response of mechanical and electronic properties of graphane to the elastic strain. *Appl. Phys. Lett.*, 96(9):091912, Mar 1, 2010.
86. M. S. C. Mazzoni, R. W. Nunes, S. Azevedo, and H. Chacham. Electronic structure and energetics of layered structures. *Phys. Rev. B*, 73(7):073108, 2006.
87. K. N. Kudin, G. E. Scuseria, and B. I. Yakobson. bn, and c nanoshell elasticity from ab initio computations. *Phys. Rev. B*, 64(23):235406, 2001.
88. E. Hernandez, C. Goze, P. Bernier, and A. Rubio. Elastic properties of c and bxcynz composite nanotubes. *Phys. Rev. Lett.*, 80(20):4502, May 18, 1998.
89. G. N. Greaves, A. L. Greer, R. S. Lakes, and T. Rouxel. Poisson's ratio and modern materials. *Nat. Mater.*, 10(11):823–837, Nov 2011.
90. J. F. Nye. *Physical Properties of Crystals*. Oxford Science Publications, Oxford, 1995.
91. S. Yu Davydov. Third order elastic moduli of single layer graphene. *Phys. Solid State*, 53(3):665, Mar 2011.